Pre-flight Calibration of the Prototype Nuclear Compton Telescope

Jason D. Bowen[a], Mark E. Bandstra[a], Steven E. Boggs[a,b], Wayne Coburn[a], Cornelia B. Wunderer[a], Robert P. Lin[a,b], Mark Amman[c], Paul N. Luke[c], Morgan T. Burks[d], William Craig[d], Norman W. Madden[d], David M. Smith[e], Peter von Ballmoos[f], Pierre Jean[f]

[a]Space Sciences Laboratory, University of California, Berkeley, CA 94720, USA
[b]Department of Physics, University of California, Berkeley, CA 94720, USA
[c]Lawrence Berkeley National Laboratory, University of California, Berkeley, CA 94720, USA
[d]Lawrence Livermore National Laboratory, University of California, Livermore, CA 94550, USA
[e]Department of Physics, University of California, Santa Cruz, CA 95064, USA
[f]Centre d'Etude Sptiale des Rayonnements, CNRS/UPS, BP 4346, 31029 Toulouse Cedex, France

ABSTRACT

The Nuclear Compton Telescope (NCT) is a balloon-borne soft gamma-ray (0.2 MeV–10 MeV) telescope designed to study astrophysical sources of nuclear line emission and polarization. A prototype instrument was successfully launched from Ft. Sumner, NM on June 1, 2005. The NCT prototype consists of two 3D position sensitive High-Purity-Germanium (HPGe) strip detectors fabricated with amorphous Ge contacts. The novel ultra-compact design and new technologies allow NCT to achieve high efficiencies with excellent spectral resolution and background reduction. Energy and positioning calibration data was acquired pre-flight in Fort Sumner, NM after the full instrument integration. Here we discuss our calibration techniques and results, and detector efficiencies. Comparisons with simulations are presented as well.

Keywords: Germanium detectors, Compton telescopes, gamma-ray spectroscopy, gamma-ray polarization, balloon payloads

1. INTRODUCTION

The Nuclear Compton Telescope (NCT) is a soft γ-ray (0.2 MeV–10 MeV) Germanium Compton Telescope (GCT) consisting of multiple High-Purity Germanium (HPGe) strip detectors, or GeDs, optimized to study astrophysical sources of nuclear line emission through spectroscopy and imaging. The principles of GCT operation have been discussed by a number of authors.[1,2] Photon interactions in the MeV energy band are dominated by Compton scattering, and for totally absorbed photons with at least two (spatially resolved) interactions, the incident photon direction can be determined to within an annulus on the sky using the Compton scatter formula,

$$\cos\phi = 1 + \frac{1}{E_0} - \frac{1}{E_1}, \tag{1}$$

where E_0 is the incident photon energy and E_1 is the photon energy after the first scatter, both normalized to the electron rest mass energy, 0.511 MeV. For proper event reconstruction, each individual photon interaction must be resolved in both position and energy space, and the correct sequence of interactions determined. The events can then be processed for the purpose of performing spectroscopy, or analyzed to obtain sky maps. 3D tracking not only enables Compton imaging, but also allows for greater background rejection through Compton Kinematic Discrimination[3] (CKD) and polarization measurements in the 0.2 MeV-0.5 MeV range.[4]

Further author information: E-mail: jdbowen@ssl.berkeley.edu, Telephone: +1−510−643−9636

Space Telescopes and Instrumentation II: Ultraviolet to Gamma Ray, edited by Martin J. L. Turner, Günther Hasinger, Proc. of SPIE Vol. 6266, 626625, (2006)
0277-786X/06/$15 · doi: 10.1117/12.672252

NCT was launched from Ft. Sumner, NM on June 1, 2005 17:06:00 UTC. The flight was terminated on June 2, 2005 01:14:22 UTC ∼166 km southwest of Albuquerque, NM. The average altitude at float was 40250 m. The duration of the flight, from launch to termination was ∼8 hours and 15 minutes. Approximately 5.5 hours of observation time (uncorrected for deadtime) was acquired at float. We are finalizing our detailed calibrations for optimal analysis of this flight data.

The NCT detectors are custom 15-mm thick cross-strip GeDs of active area 5400 mm^2 each. Orthogonal 37×37 2-mm pitch electrode strips on the opposite faces, combined with signal timing, provide full 3D position resolution to 1.6 mm^3. A gap of 0.25 mm between the strips has been demonstrated by LNBL to minimize the number of charge sharing events and the resulting charge loss, while maintaining the high GeD spectral resolution. A 2-mm thick guard ring surrounds this active area on both faces of the detector, with a 1 mm gap between the ring and the edge of the crystal. The guard rings are instrumented to provide anticoincidence signals for rejection of events with interactions in these regions. The strips are instrumented both the ground (DC coupled, anode) and HV (AC coupled, cathode) sides with custom low power, low noise preamplifiers.

The NCT 3D-GeDs operate as fully depleted p-i-n junctions, using amorphous Ge contact technologies pioneered by LBNL.[5] In this technique, the blocking electrode is made from a ∼0.1-μm thick layer of amorphous Ge deposited on the entire detector surface. This amorphous film serves as the blocking contact, and fully passivates every detector surface not used for contact connection. The amorphous germanium can be made highly resistive which provides excellent inter-electrode impedance,[6] which has been demonstrated to significantly improve the charge collection for events that occur in the inter-strip region, and allows for excellent spectroscopy even when charge is shared by neighboring strips.[7]

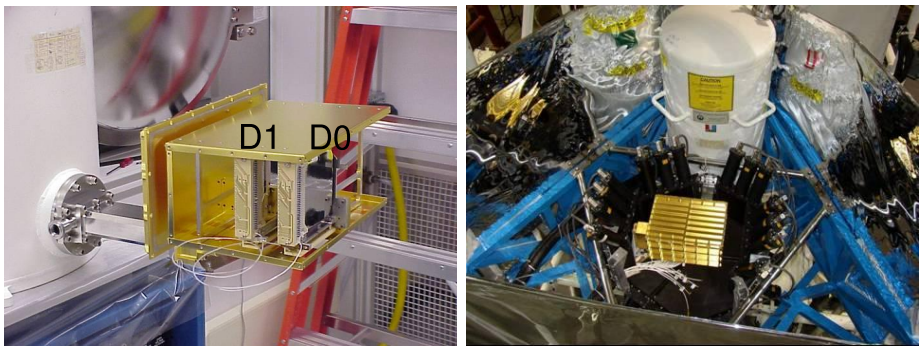

Figure 1. LEFT. The two GeDs, D0 and D1, are attached to a copper coldfinger. Surrounding them on the top and bottom is the partially assembled IR shield. The detectors in this figure are spaced 2" center to center. For the actual flight, the spacing was 1" center to center. RIGHT. The cryostat (gold) containing the two GeDs sits in an active BGO well. In the rear resides the liquid nitrogen dewar. On the sides are pieces of the sun shield.

For this flight, NCT was configured with 2 GeDs, but can be configured with up to twelve detectors. (The full 12-detector array will be flown from Alice Springs, Australia in December 2008 and 2010.) The 2 GeDs are situated in an evacuated gold-plated aluminum cryostat and are mounted on a copper coldfinger maintained at 85 K through contact with liquid nitrogen held in a 50 L dewar (see Figure 1). Active shielding is provided by a BGO well that surrounds the detectors on all sides except for the forward and zenith directions.

The NCT prototype instrument consists of two GeDs arranged as shown in Figure 1. In the figure, D0 has an open view of the forward and zenith directions and D1 is positioned directly behind D0. The strip electrodes comprise an orthogonal set defining 37×37 cross-strip pairs, or 'pixels,' for the determination of the 2D interaction positions. When a γ-ray interacts in a detector, an energetic recoil electron is produced that raises nearby electrons from the valence band into the conduction band, leaving holes behind. The electrons and holes drift in opposite directions under the influence of the electric field and are collected at the appropriate strips. Due to the finite drift velocities of the electrons and holes, the charge Collection Time Difference (CTD) can be measured, effectively determining the remaining position coordinate. Given the measured 3D positions

of the interactions and the corresponding energies, Compton kinematics may be applied to obtain the incident photon direction to within an annulus on the sky.

The induced signal due to the motion of the charge carriers is extracted with custom charge-sensitive preamplifiers and then further processed by both a slow and fast channel. The slow channel (4.2-4.6 μs time to peak), or spectroscopy channel, is followed by a peak detect and 13-bit (8192 channel) Analog-to-Digital Converter (ADC). The fast channel, a delay line ($\sim$200 ns) constant fraction discriminator, time stamps each input pulse at 50% the maximum amplitude, facilitated with a 100 MHz clock. The digitized pulses and time stamps are matched to their corresponding strips and are passed along the data stream to be stored and/or telemetered to the ground for later processing.

The energy information of a photon interaction is contained in the Pulse Height Amplitude (PHA) as given by the value of the analog-to-digital conversion. The relationship between energy and PHA value is approximately linear and varies from strip to strip due to variations of amplifier gain and delay line offset. (A dedicated signal processing chain follows each of the 2×2×37 strip electrodes.) The depth of the interaction is extracted by matching active DC and AC strips and taking the difference of their time stamps. (We do not possess the time resolution, the light travel time across the length of a detector, to match active strips through timing, so we rely on spectroscopy.) The relationship between the CTD and depth is also approximately linear, with an offset introduced by the differences in drift velocities of the electrons and holes in the presence of an electric field. The intersection of the AC and DC strips define 37×37 surface 'pixels,' each with unique CTD calibrations. This paper is a discussion of the energy and depth calibration techniques employed to convert the measured parameters (PHA value and time stamp), into meaningful physical values (energy and depth of interaction).

2. ENERGY CALIBRATIONS

Nuclear astrophysics is the study of the lifecycle and evolution of matter in our Universe: stellar evolution ending in supernovae (SNe), with the ejection of heavy nuclei back into the galaxy to be reborn in new stars. Radioactive nuclei produced in this cycle of creation emit characteristic photons that fingerprint the isotopes themselves, and quantify their abundances and kinematics. The proper determination of these photon energies is essential for nuclear line science and for optimizing Compton imaging. Accurate measurements of photon energies and line shapes probe deep into the center of a SN explosion, revealing the nuclear burning and dynamics in the core. Radioactive nuclei and positrons also reflect the extreme environment on the surfaces of neutron stars and white dwarfs, and near the event horizon of black holes. Correctly interpreting the results of the science data gathered from these sources requires an accurate energy calibration of the instrument.

Calibrations are performed by measuring the positions of known lines. Table 1 lists the sources we used for our calibrations and the energies of the prominent lines. A linear fit gives good results at high energies (see Figure 2), but fails at lower energies. The left-hand side of Figure 3 shows that a purely linear calibration mimics charge loss at low energies, and leads to significant tailing.[8] A more sophisticated fit is required to account for the nonlinear behavior at low energies. The right-hand side of Figure 3 shows our results from a 5th order polynomial fit to the calibration data.

Sources of nonlinear response in our detector system include the intrinsic nonlinear response of germanium, and the pulse-shaping elements of the slow channel. A few authors have investigated the linear response of Ge(Li) detectors, and found deviations from linearity of less than 0.3% in the 0.06 MeV–3 MeV range[9] and in some cases less than 0.046% in the range 0.5 MeV–10 MeV.[10] Zulliger et al.[9] have argued that an intrinsic departure of 0.1% in silicon at low energies ($\sim$2 keV) is unavoidable due to the finite energy required for the creation of an electron-hole pair ($\sim$4 eV for silicon). For germanium the result is somewhat less given that the energy needed for the creation of an electron-hole pair is smaller (2.96 eV). In fact, departures from linearity as large as 2%[11] are observed in Ge near the K absorption edge (11.103 keV), and are due to a possible energy dependence of the electron-hole pair creation energy at these low energies, to trapping effects, or a combination of both. The importance here is that from 60 keV to 3 MeV the energy response of germanium is linear to within 0.3%, an upper limit to the observed energy resolution in NCT, and improves with increasing energy.

Five radioactive sources were used to calibrate the instrument pre-flight: ^{241}Am, ^{57}Co, ^{133}Ba, ^{137}Cs, and ^{60}Co, yielding nine lines (see Table 1). A spectrum was acquired for all sources in the on-axis position 580 cm from

Table 1. Calibration source characteristics.

Source	Line Energy (keV)	Branching Fraction (%)	Activity (μCi)	Date	On-axis Exposure (ks)	Total Exposure (ks)
^{241}Am	59.5	36	1000	10 May	6.208	6.208
^{133}Ba	81.0	34	60	4 May	9.283	42.470
	276	7.1				
	303	18				
	356	62				
^{57}Co	122	86	17	10 May	9.089	9.089
^{137}Cs	662	85	84.6	3 May	11.298	23.560
^{60}Co	1173	100	40	4 May	6.862	50.738
	1333	100				

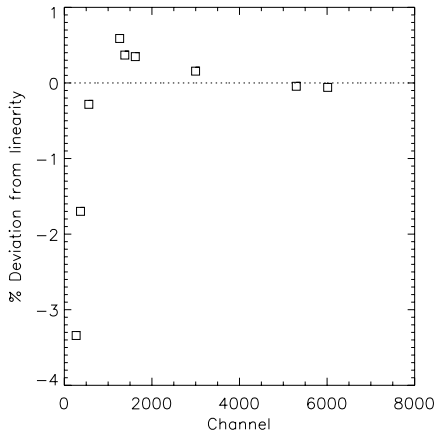

Figure 2. The percentage difference between a purely linear calibration and the known energies for the nine line energies listed in Table 1 for D0 AC strip 4. This plot makes apparent the shortcomings of a purely linear calibration.

the D0 body center. Also, for ^{133}Ba, ^{137}Cs, and ^{60}Co, energy spectra were acquired at four additional elevations: 17.6°, 28.6°, 38.0°, and 49.9° with source distances of 591 cm, 628 cm, 685 cm, and 808 cm, respectively.

We calibrated D0 using the five sources listed in Table 1, yielding nine usable lines that span the energy range 0.060 MeV–1.3 MeV. We used a 5th-order polynomial to fit the data acquired for both the anode and cathode sides of D0. Figure 4 shows the nuclear line positions for AC strip 7. The large errors in the ^{60}Co lines are due to poor statistics at these energies. Even though there are considerable uncertainties in the line positions at 1.17 MeV and 1.33 MeV, weighted fits give accurate results due to the excellent linear response of Ge at higher energies (Figure 2).

Only five nuclear lines above 276 keV were usable as energy calibration sources for D1 due to significant attenuation in D0. At 276 keV, the total scattering cross-section in Ge is 0.11 cm^{2}g^{-1}, i.e., approximately 42% of the original beam is available to D1. Of these photons, 58% will interact, of which only about 16% are photoabsorbed events. The ^{133}Ba source activity at 276 keV is 4.6 μCi. At 580 cm, the expected number of photoabsorbed 276 keV photons for an 8 hour acquisition period is ∼45, or about 1.2 per strip. At lower photon energies, the photoabsorption cross section increases and D0 is more effective at stopping photons. Positioning the source antiparallel to the on-axis direction for direct D1 illumination, or even at oblique angles, was considered. However, difficulties with attenuation remained at low energies due to the presence of nearby passive material (in particular the 50 L liquid nitrogen dewar) and oblique configurations introduced difficulties with characterizing the source geometry accurately. Another challenge present with oblique configurations is the loss of uniform

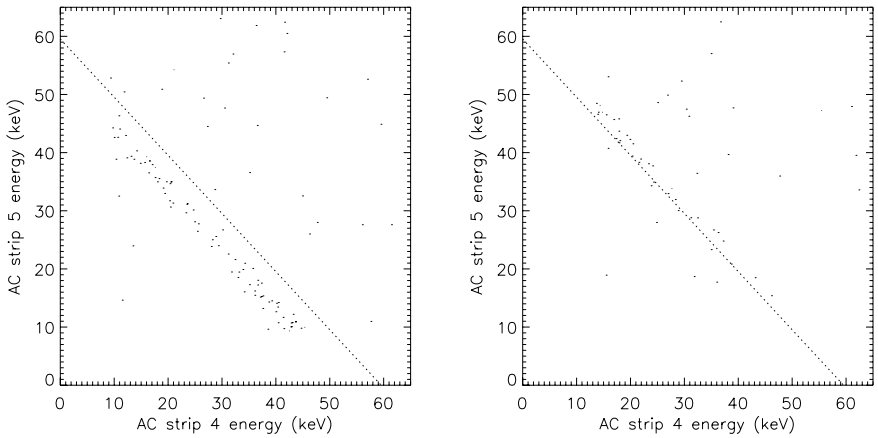

Figure 3. LEFT. A purely linear calibration does not account for nonlinearities at low energies. Here, charge sharing at 60 keV (^{241}Am) mimics charge loss between D0 AC strips 4 and 5 . RIGHT. In this plot we use a 5th order polynomial to fit the calibration data (Table 1). The nonlinearities are corrected with this fit.

detector surface illumination and significant shadowing due the presence of gondola structures.

Due to the challenges recently discussed, nuclear lines with energies below 303 keV (^{133}Ba) were not available for calibrating D1. Calibrations relying on the remaining lines, without accounting for the nonlinear behavior at lower energies, leads to significant tailing below lines in this energy range and greater uncertainty in line positions. A nonconventional energy calibration approach was used for D1 that relies on the excellent intrinsic linear response of germanium in our energy range of interest. A step pulse of unknown but constant amplitude was input into the slow channel after passage through a precision attenuator. By adjusting the attenuator, approximately 20 points, spaced by 2 dB and spanning the ADC range ∼100–7500, were accumulated for each channel–corresponding to an energy range of roughly 20 keV–1300 keV. We fit the digitized pulser inputs with a 5th-order polynomial. These polynomials serve as calibration templates, matching ADC channels to pulse amplitudes. If the response of the Ge and preamplifier system were linear, then the pulse amplitudes could be scaled to a single line of known energy and channel position by multiplication with a suitable normalization factor. We do not need to know the absolute values of the pulse amplitudes, but only the relative spacing, which is 2 dB. If $f_5(P)$ is the 5th order polynomial fit to the pulser data, then the energy calibration is given by

$$E = \xi f_5(P), \tag{2}$$

where $\xi = E_0/f_5(P_0)$, the normalization factor, is the ratio of a known line energy and its corresponding pulse amplitude at the PHA value P_0. In general the normalization factor is not constant, but varies according to the nonlinearities present in the detector-preamplifier system (see Figure 4). We used a quadratic to account for the variation of ξ with energy, where now the energy calibration is given by

$$E = \xi_2(P) f_5(P). \tag{3}$$

$\xi_2(P)$ is a 2nd order polynomial giving the normalization factor as a function of PHA value. The bottom right hand side of Figure 4 shows the residuals using this technique. Of course, using calibration data to generate calibration templates gives better results, as we did with D0, but with less confidence at lower energies.

The absence of significant background lines for this flight leads to improved instrument sensitivity, however, we are required to rely on calibration data acquired during the weeks prior to launch. While recognizing the importance of *in-situ* calibration measurements during flight to correct for electronic drift, at the present time no measurements are available due to the absence of in-flight calibration sources and a dearth of narrow background lines with sufficient statistics. Historically, in-flight spectral calibrations were possible for large coaxial GeDs due to the presence of bright background lines, but such lines are absent from the individual strip spectra in NCT. In

the presence of drift, we have observed nuclear lines to shift by as much as 0.2% over the course of a day, while similar variations have been observed in HIREGS[12] on day-night time scales, confirming the strong temperature dependence of system drift. At float, the system temperature was stable to within 4° C, and electronic drift is not expected to be an important factor for this flight. However, system drift must be characterized to account for line shifts between the calibration data acquisition period and the actual flight. We believe such a correction is possible if significant background lines can be found in the single strip spectra. Analysis is currently ongoing.

Figure 5 shows two spectra obtained with the AC side of D0 and the DC side of D1. D0 was calibrated by fitting the calibration data with a 5th-order polynomial. D1 was calibrated using our technique discussed above. The two lines appearing in each plot are the 1173.237 keV and 1332.501 keV ^{60}Co lines. The D0 FWHM for the two lines in the figure are 4.9 keV (0.4%) and 5.3 keV (0.4%). The corresponding FWHM for the DC side of D1 are 8.7 keV (0.7%) and 10.1 keV (0.8%). Given our single-site spectral resolutions (Figure 6), these Compton scatter resolutions are somewhat broader than expected, indicating better cross-calibrations are still required. The residual low-energy tails on these lines are primarily due to the finite threshold of our detectors (∼15 keV, but imposed uniformly at 25 keV for this plot) with perhaps a secondary contribution from charge loss between strips, which we are still in the process of characterizing.

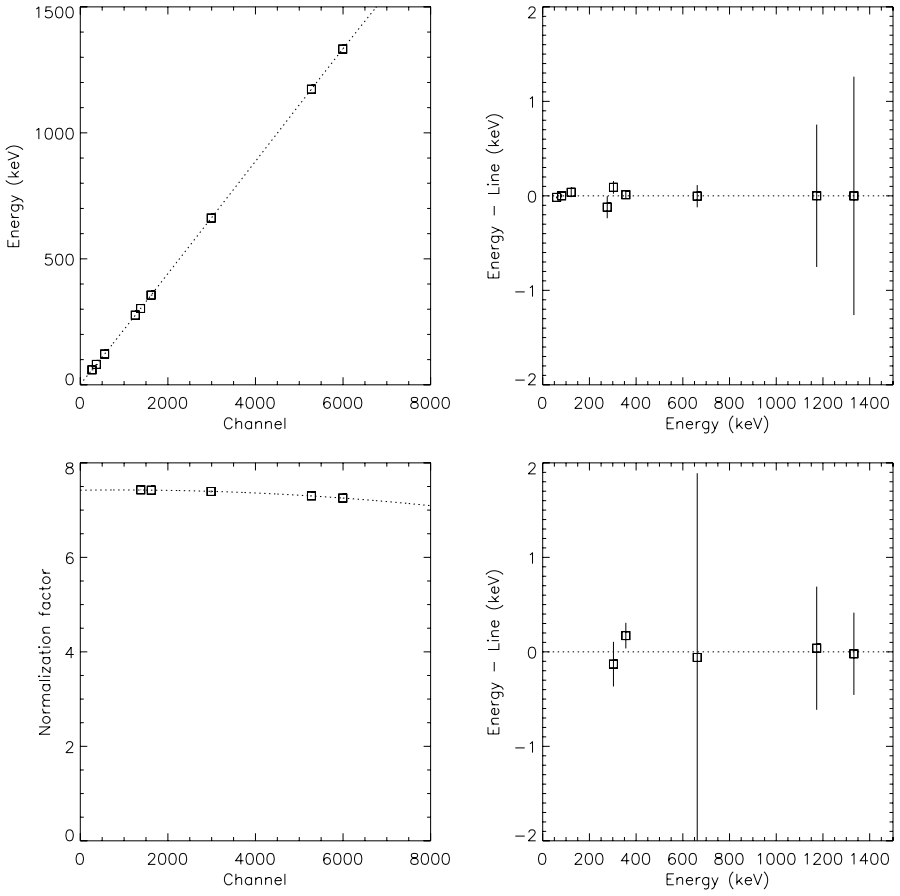

Figure 4. TOP LEFT. Plotted are all nine of the calibration points listed in Table 1 for D0 AC strip 7. The dotted line is our 5th order polynomial fit to the data. TOP RIGHT. The residuals between our fit and the known line energies. BOTTOM LEFT. The normalization factor as a function of the five nuclear lines available to D1 DC strip 35. Notice it is not constant with energy. BOTTOM RIGHT. The residuals between the energy calibration approach discussed in the text and the known line energies.

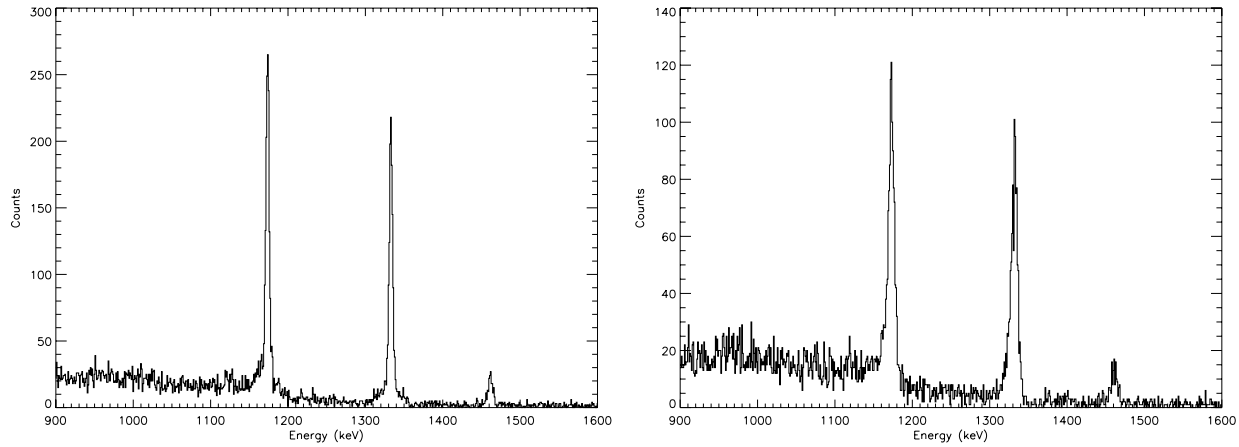

Figure 5. LEFT. ^{60}Co spectra obtained with the AC side of D0. RIGHT. The same as on the left but for the DC side of D1. Only events with two or more interactions are included (i.e., only Compton-scattered events). The line positions are: 1173.6±0.1 and 1333.1±0.4 keV (left); and 1172.8±0.4 and 1331.8±0.5 keV (right). (Uncertainties only include statistical uncertainties, not systematic.)

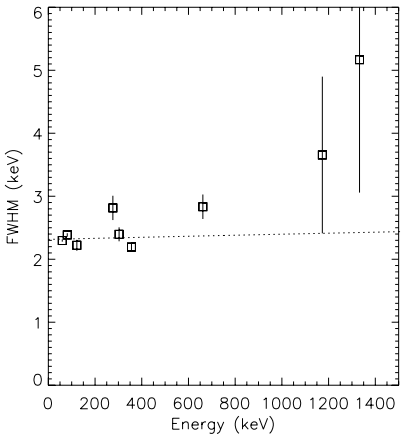

Figure 6. The single-site FWHM of D0 AC strip 7 as function of energy, E. Also shown is a model (dotted line) consisting of two contributions, a constant component (electronic noise) and a term proportional to $\sqrt{E}$, assumed to add in quadrature.

3. EFFICIENCY CALIBRATIONS

To accurately measure source flux, the instrument effective area must be accurately characterized. The effective area, A_{eff}, is defined as the collected photon event rate divided by the source photon flux at the detector, and is generally a function of energy. To confidently characterize A_{eff} in NCT, we used simulations normalized by a number of calibration points. It is usually sufficient to simulate a grid of energies and incident directions and then scale the results to the measured data. For this process to work, an accurate mass model (Figure 7) must be developed and the corresponding event cuts, thresholds, and event reconstruction algorithms must be matched.

Figure 8 shows the results obtained using a subset of the grid we employed. On the left hand side of the figure are the effective areas as a function of energy for the on-axis position. Additional lines were included that were too weak for calibrating individual strips. The largest discrepancies between our measured data and the simulations are at low energies. For the plot on the right in Figure 8, ^{137}Cs (662 keV) is simulated. The polar

angle varies from on-axis (0°) to zenith (90°). Measured data is also shown. Some discrepancies are apparent, but the results are encouraging at this early stage of the analysis. Detailed analysis of efficiencies for various data cuts is ongoing.

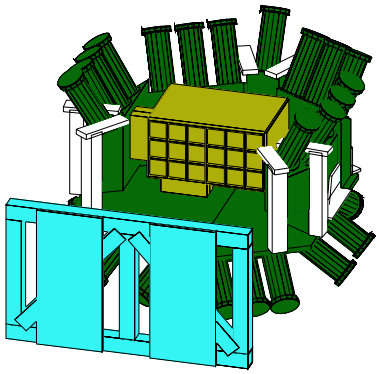

Figure 7. The NCT mass model. The GeDs (not shown) are housed inside the cryostat. The preamplifier boxes on the left side and bottom of the cryostat can be seen, and the shield modules and photomultiplier tubes are clearly visible. A section of the 'cradle' is situated 43 cm in front of the cryostat. It is a significant source of passive material and influences the on-axis measurements.

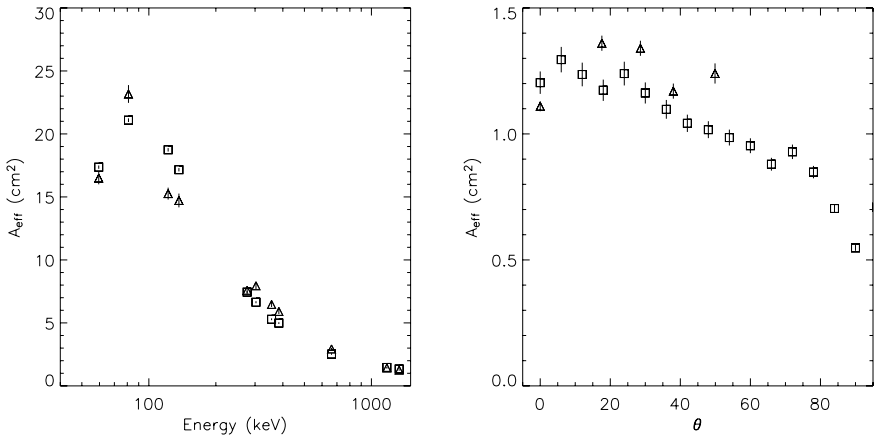

Figure 8. LEFT. Simulated on-axis photopeak effective areas (squares) compared with lab measurements (triangles). The largest discrepancies exist at 122 keV and 136 keV (^{57}Co) and may reflect an error in the reported source activity. Good agreement is seen at higher energies. In this plot, additional lines are included that are not listed in Table 1: 136 keV (^{57}Co) and 384 keV (^{133}Ba). The mass model shown in Figure 7 was used for these simulations. RIGHT. Simulated effective area (squares) as a function of angular distance from on-axis for ^{137}Cs (662 keV), and measured data (triangles), for a subset of photopeak events that scattered between D0 and D1. The discrepancies close to on-axis may, in part, be due to the exclusion of gondola structures in the simulations.

4. DEPTH CALIBRATION

Our compact Compton telescope design requires full 3D positioning to optimize the Compton imaging performance. The full 3D position of an interaction is determined by identifying the active cross-strip pair, or 'pixel,' and by determining the depth, or z-, component of the interaction. The z-coordinate cannot be measured directly, but is inferred from the Collection Time Difference (CTD), defined as the difference between the signal

half-rise times of the DC and AC sides. Depth calibration requires the determination of the relationship between the CTD and the z-coordinate of the interaction, which is approximately linear. Ideally, the calibration is determined by measuring the CTD of photons of known interaction depth, which is not possible. Instead, known depth *distributions* are employed.

The primary depth calibrations were performed using ^{137}Cs (662 keV). The large mean free path in germanium of 662 keV photons allows one to probe both edges of both detectors simultaneously, an advantage given that uniform illumination of all sides was not possible due to the physical constraints imposed by the detector geometry. However, a disadvantage with ^{137}Cs is the low photoabsorption rate, which requires us to use more clever event selection (rather than just using the photopeak events) in order to obtain enough usable data.

The event selection we used for the preliminary calibrations described here is to select single-site events with energies between 400 and 480 keV, and single-site photopeak events within 10 keV of 662 keV. These cuts were chosen both for their simplicity and in order to select portions of the single-site event energy spectrum that were not background-dominated. The region of 400-480 keV is the Compton edge for 662 keV photons, where photons backscatter once and leave the detector. Performing this event selection on the calibration data, the CTDs are measured and stored for later comparison to simulations. In this way, a library containing CTD distributions for each pixel is created.

Simulations are used to connect the known detector physics to the measured CTD histograms for each pixel. We perform Monte Carlo simulations of the calibration data runs and determine the resulting CTD histogram shape. Photon interactions were simulated using the MGEANT Monte Carlo package and the NCT mass model. The interaction positions are stored, and the resulting electron and hole drift is simulated using a custom charge transport package. Given the electron and hole cloud positions and velocities as a function of time, the induced current on the strip electrodes can be calculated,[12,13] and a simulated CTD distribution can be reconstructed. Figure 9 shows the Monte Carlo depth distributions for both GeDs, and Figure 10 shows the resulting CTD histograms. Notice the edge effects and the bump at CTD=0 in the CTD histograms. The edge effects have been seen before in similar simulations, but the feature at CTD=0 is still under investigation. These simulated CTD histograms are used as templates to calibrate the individual detector pixels.

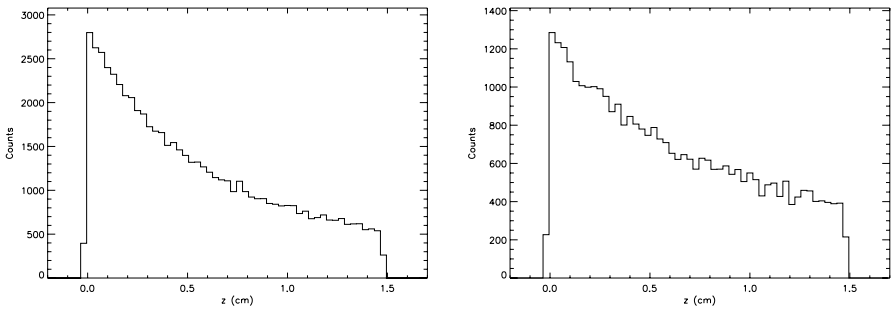

Figure 9. The simulated depth distribution of events from the Monte Carlo simulations for D0 (left) and D1 (right). As expected, the curves are approximately exponentials.

Simulations are used a second time to connect measured CTD to depth z. We determine the z-CTD relationship by charge transport simulations of a flat depth distribution. A plot of depth versus CTD is given in Figure 11. These points were calculated using a flat depth distribution sampled at regular intervals but spread across the cross-strip area. The CTD has already been shown to be linear with depth to first order.[7,13] We perform a quadratic fit to the z-CTD scatterplot (Figure 11) to accurately reproduce the nonlinearities near the edges. In addition, the spread of points around our polynomial fit allows us to estimate our intrinsic error in depth, which we describe below.

Each pixel of the detector must be individually calibrated. These calibrations are performed assuming the shape of the simulated CTD histogram is correct. Measured CTD values are then taken to be linear

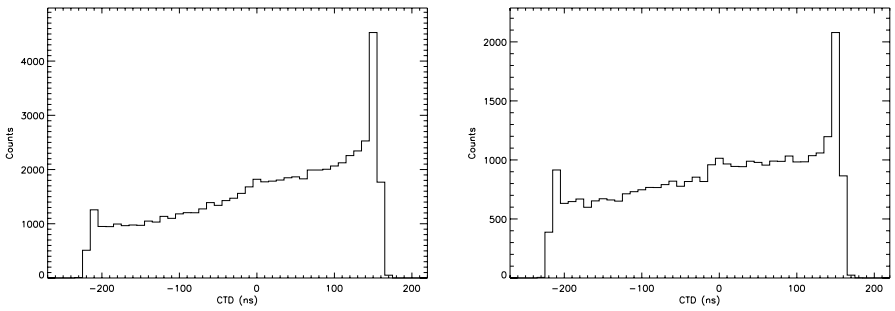

Figure 10. Simulated CTD histograms for the depth distributions obtained from the Monte Carlo simulations. The histograms shown here are for D0 (left) and D1 (right). Note the edge effects on each histogram and the slight bump at CTD = 0. These CTD histograms are used as templates to fit the individual detector pixels.

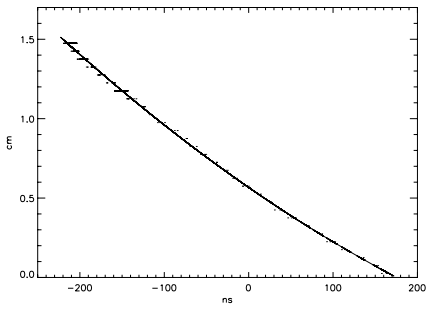

Figure 11. A scatterplot of depth (vertical axis) versus CTD (horizontal axis). For the data shown here, the simulated points were evenly distributed at regular intervals in depth. The curve is a quadratic fit to the scatterplot.

transformations of the calibrated "true" CTD values, i.e.,

$$\tau_0 = \eta\tau + \Delta\tau, \tag{4}$$

where τ_0 is the calibrated CTD, and τ is the measured CTD. The factor η (which is of order 1) is a stretching factor to account for field, hence drift velocity, variations across the detector. $\Delta\tau$ is a time offset to account for slight variations in absolute timing between strip electronics. A template of the simulated CTD histogram for a given calibration run is made from the simulations described previously. The template is then fit to the measured CTD histogram for each individual pixel to determine the calibration parameters η and $\Delta\tau$. An example is shown in Figure 12. Once the two calibration parameters are determined for each pixel, the measured CTD can be calibrated and the depth can be determined using the z-CTD relation found from the data in Figure 11.

A posteriori justification of this depth calibration method is obtained by checking the performance over the entire detector. One can create a coadded CTD histogram for a detector by applying the two calibration parameters η and $\Delta\tau$ to transform from the measured CTD to the calibrated CTD. The resulting histograms, along with the uncalibrated CTD data, are shown in Figure 13. Notice the emergence of sharp features at the edges, as expected from the shape of the individual pixel CTD histograms and the simulated CTD histograms. The feature at CTD=0 also appears, although it is sharper than the the feature seen in the simulations. The cause of this feature is not yet well understood, nor is it known why it appears so sharp in the calibrated data.

One goal of the depth calibration is to determine the noise level of the electronics, believed to be about 10 ns FWHM. To justify this noise level, we can compare the coadded CTD histogram to the simulated CTD template convolved with different noise levels. Such a comparison is made in Figure 14. One can easily see from the edge features alone that the noise level is probably at most 10-15 ns FWHM, corresponding to depth uncertainties of 0.4-0.6 mm FWHM. Future analysis is planned for a more quantitative comparison.

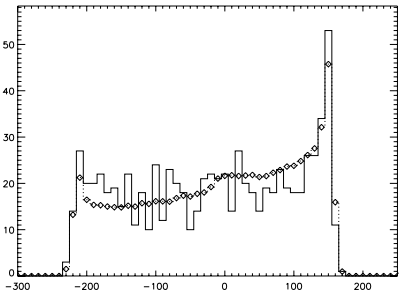

Figure 12. An example of a template fit to an individual pixel, in this case AC 9 DC 6 on D0. The data is shown with a solid line, while the CTD template fit is overplotted with dots.

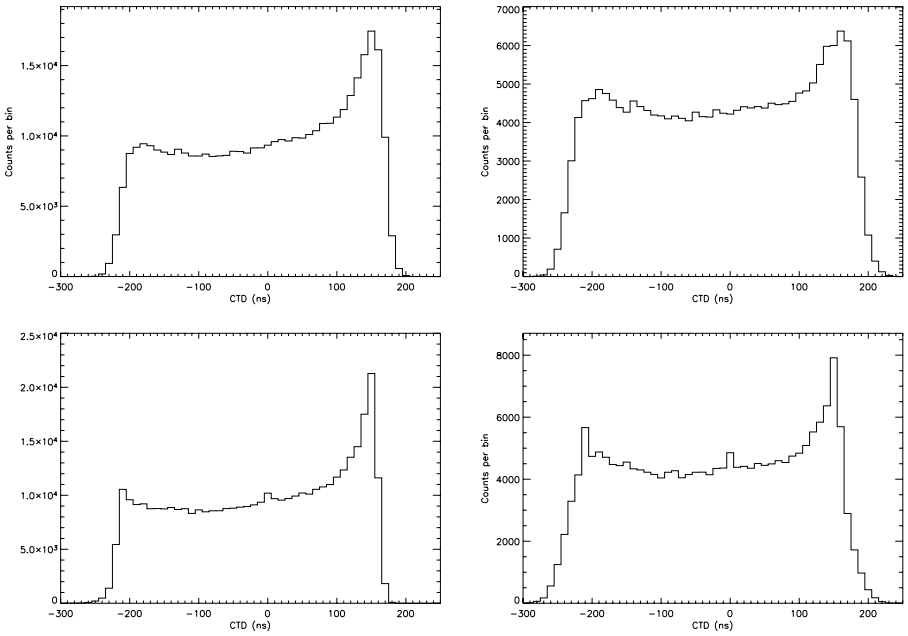

Figure 13. Coadded CTD histograms for the entire detector. The top row shows histograms of the raw CTD data for all pixels in D0 (top left) and D1 (top right). The bottom row shows histograms of the calibrated CTD data for D0 (lower left) and D1 (lower right). Notice the emergence of sharp features at the edges and at CTD = 0. The calibration for D1 is not as good as the calibration for D0, as can be seen by the spread in its calibrated CTD histogram.

The simulations have also been used to quantify the intrinsic error in the depth calibration. It is easily seen from Figure 11 that there is a spread around the fitted z-CTD function. This spread results from the distribution of simulated points in the x-y plane and the nonuniformity of the field in the x-y direction. Another contributor to the intrinsic error is the 10 ns resolution of the electronics. In order to determine the intrinsic error, 10 ns-wide intervals of CTD data from the flat depth distribution simulations (e.g., Figure 11) were analyzed and the intrinsic rms uncertainty in depth as a function of CTD was calculated. This error is shown in Figure 15.

5. FUTURE DIRECTIONS

Our primary goals for the NCT prototype calibrations and flight are to characterize the effective areas, field-of-view, angular resolutions, background, and sensitivity. All of these performance characteristics depend strongly

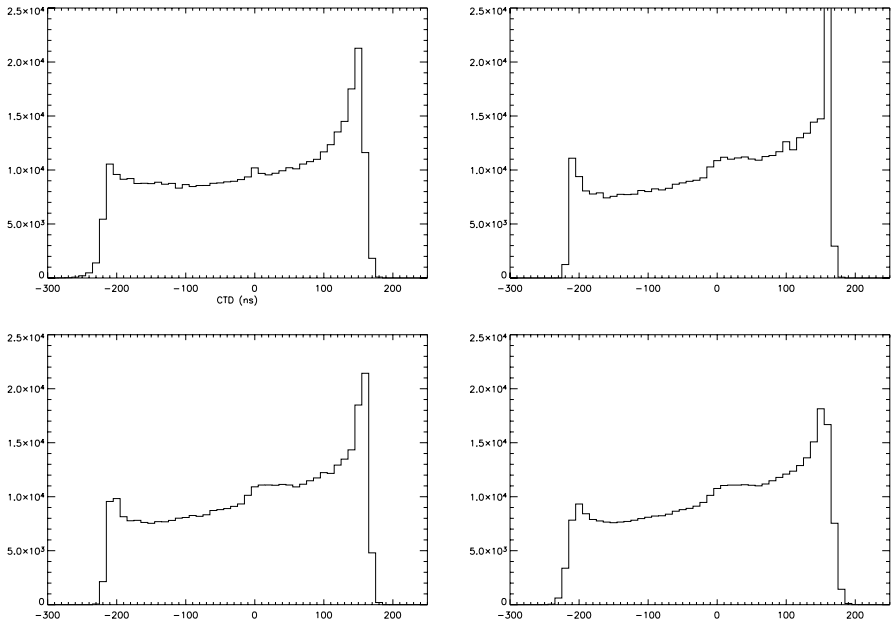

Figure 14. Investigation of noise levels in D0. The calibrated coadded CTD histogram for D0 (upper left) is compared to the D0 template with no noise (upper right), convolved with 10 ns FWHM noise (lower left), and convolved with 20 ns FWHM noise (lower right). Our estimated noise level of 10 ns FWHM compares favorably to the template with the same noise level.

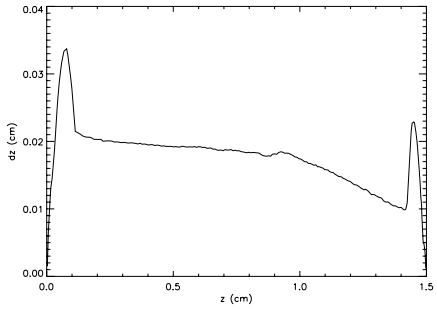

Figure 15. Intrinsic error in depth as a function of depth. As expected, the edge effects create correspondingly large errors at the surfaces of the detector.

on event selections, which in turn require careful energy and position calibrations. Our first comparisons between measured and simulated efficiencies presented here are encouraging, but much more work is required on these high-level performance characteristics. The detailed spectral and positioning calibrations presented here will let us move forward in these goals.

Though the technique used to calibrate D1 gives results not as good as a single fit to the calibration data, the results are acceptable in light of the goals of this flight. Data analysis on the measured background and the 511 keV positron annihilation line is ongoing and results are expected soon. Future flights with the 12-GeD instrument are planned for December 2008 and 2010 flight seasons from Alice Springs, Australia. For that flight an extensive grid of energies and incident source directions will be used. The mass model will be improved, and possibly a weak in-flight calibration source will be flown with the instrument.

The depth calibration is a work in progress. We are optimizing the event selection to increase the number of

usable interactions and to decrease the amount of background. Presently, all single-site events between 400 and 480 keV are chosen along with photopeak events, and no background rejection is performed. Instead of these simple cuts, we might use Compton kinematic discrimination[3] to choose good events and reject background. This method would also allow us to use the many multiple-site events that so far have been ignored. Increasing the number of usable events will also aid in improving the calibration of D1, which suffered from attenuation by D0. For subsequent flights, longer data runs will be performed to be assured of having plenty of photons.

One last note is that our study of the error in the depth calibration has only used simulations, and therefore only provides an estimate of the intrinsic error, not the systematic error. Once the depth calibration itself is improved, we can further investigate the systematic errors of our procedure.

REFERENCES

1. P. von Ballmoos, R. Diehl, and V. Schonfelder, "Imaging the gamma-ray sky with compton telescopes," *Astron. Astrophys.* **221**, pp. 396–406, 1989.
2. S. E. Boggs and P. Jean, "Performance characteristics of high resolution compton telescopes," *Astron. Astrophys.* **376**, pp. 1126–1134, 2001.
3. S. E. Boggs and P. Jean, "Event reconstruction in high resolution compton telescopes," *Astron. Astrophys. Suppl. Ser.* **145**, pp. 311–321, 2000.
4. S. E. Boggs, W. Coburn, D. M. Smith, J. D. Bowen, P. Jean, J. M. Kregenow, R. P. Lin, and P. von Ballmoos, "Overview of the Nuclear Compton Telescope," *New Astron. Rev.* **48**, pp. 251–255, Feb. 2004.
5. P. N. Luke, C. P. Cork, N. W. Madden, C. S. Rossington, and M. F. Wesela, "Amorphous ge bipolar blocking contacts on ge detectors," *IEEE Trans. Nucl. Sci.* **39**(4), 1992.
6. P. Luke, R. Pehl, and F. Dilmanian, "A 140-element Ge detector fabricated with amorphous Ge blocking contacts," *IEEE Trans. Nucl. Sci.* **41**, pp. 976–978, 1994.
7. M. Amman and P. N. Luke, "Three-dimensional position sensing and field shaping in orthogonal-strip germanium gamma-ray detectors," *Nucl. Instrum. Methods Phys. Res., Sect. A* **452**, pp. 155–166, 2000.
8. W. Coburn, S. E. Boggs, S. Amrose, R. P. Lin, M. T. Burks, M. Amman, P. N. Luke, N. W. Madden, and E. L. Hull, "Results of charge sharing tests in a ge-strip detector," *IEEE Nuclear Science Symposium Conference Record (Cat. No.01CH37310)* **1**, pp. 226–229, 2002.
9. H. R. Zulliger and D. W. Aitken, "Charge collection efficiencies for lithium-drifted silicon and germanium detectors in the x-ray energy region," *IEEE Trans. Nucl. Sci.* **15**(1), pp. 466–474, 1968.
10. A. J. Levy and R. C. Ritter, "Linearity of a ge(li) detector in the range 0.5 to 10 mev," *Nucl. Instrum. Methods Phys. Res.* **49**, pp. 359–360, 1967.
11. H. R. Zulliger, L. M. Middleman, and D. W. Aitken, "Linearity and resolution of semiconductor radiation detectors," *IEEE Trans. Nucl. Sci.* **16**(1), pp. 47–61, 1969.
12. S. E. Boggs, *Gamma Ray Spectroscopy: Galactic Center Observations and Germanium Detector Development.* PhD thesis, University of California, Berkeley, University of California, Berkeley, CA, 1998.
13. S. Amrose, S. E. Boggs, W. Coburn, G. Holland, R. P. Lin, and D. M. Smith, "Numerical simulations of 3d positioning in cross-strip ge detectors," *2001 IEEE Nuclear Science Symposium Conference Record (Cat. No.01CH37310)* **1**, pp. 230–233, 2002.